International Journal of Industrial Chemistry (2019) 10:77–87
https://doi.org/10.1007/s40090-019-0173-8

RESEARCH

Graphene oxide–$Fe_2V_4O_{13}$ hybrid material as highly efficient hetero-Fenton catalyst for degradation of methyl orange

Inbasekaran Muthuvel[1,2] · Kaliyamoorthy Gowthami[1] · Ganesamoorthy Thirunarayanan[1] · Palusamy Suppuraj[1] · Balu Krishnakumar[3] · Abílio José Fraga do Nascimento Sobral[3] · Meenakshisundaram Swaminathan[4]

Received: 22 February 2018 / Accepted: 13 February 2019 / Published online: 21 February 2019

Abstract

A new hetero-Fenton type GO/$Fe_2V_4O_{13}$ was developed and characterized by FT-IR, XRD, HR-SEM, TEM, and UV-DRS analysis. XRD pattern reveals the presence of monoclinic phase of $Fe_2V_4O_{13}$ in the catalyst. TEM images show the particle sizes in the range from 20 to 100 nm and the nice dispersion of nanosized $Fe_2V_4O_{13}$ particles on the surface of the graphene oxide. The hetero-Fenton catalyst was used for the degradation of Methyl orange (MO) under UV and solar light. The mineralization rate was influenced by H_2O_2 concentration, pH, and catalyst loading. The reusability 21% GO/$Fe_2V_4O_{13}$ was analyzed. GO/$Fe_2V_4O_{13}$ was stable and reusable up to five cycles with 95% degradation. Solar experiments were carried out at different initial solution pH with $Fe_2V_4O_{13}$ and 21% GO/$Fe_2V_4O_{13}$. Both catalysts show maximum degradation efficiency at pH 6. Mechanism of heterophoto-Fenton process is also proposed. This study reveals that $Fe_2V_4O_{13}$ and 21% GO/$Fe_2V_4O_{13}$ catalysts are efficient under UV and solar light for the degradation MO and can be utilized for the treatment of dye wastewater.

Keywords $Fe_2V_4O_{13}$ · Graphene oxide · Wastewater treatment · Hetero-Fenton reaction · Photocatalysis

Introduction

In recent years, emerging contaminants in the environment have become a matter of concern for the scientists and the public. The photocatalytic degradation of various kinds of organic pollutants using semiconductor nanocomposites has been extensively studied [1–4]. Owing to its relative high photocatalytic activity, chemical stability, and nontoxic nature, TiO_2 has been widely used as a photocatalyst [5, 6]. However, the high frequency of charge–carrier recombination and the presence of a large band gap in TiO_2 impair its commercial application [7]. A comparative study on the degradation of dyes by UV/TiO_2, UV/H_2O_2, and Fenton processes revealed that the photo-Fenton process was more efficient than the other two processes [8]. The Fenton reaction produces hydroxyl radicals as a result of the reaction between Fe^{2+} and H_2O_2 and is effective in the complete destruction of organic contaminants into harmless compounds, thus removing pollutants from water [9]. However, the separation and recovery of ions become another hindrance in the application of a homogeneous Fenton reaction. To overcome these disadvantages, heterogeneous Fenton-like catalysts have been reported [10, 11]. The mechanism of the heterogeneous Fenton reaction is presented as follows:

$$Fe^{3+} + H_2O_2 \rightarrow Fe(OOH)^{2+} + H^+ \quad (1)$$

$$Fe(OOH)^{2+} \rightarrow Fe^{2+} + HO_2^{\cdot} \quad (2)$$

$$Fe^{2+} + H_2O_2 \rightarrow Fe^{3+} + OH^- + OH^{\cdot} \quad (3)$$

$$Fe^{3+} + HO_2^{\cdot} \rightarrow Fe^{2+} + H^+ + O_2 \quad (4)$$

Electronic supplementary material The online version of this article (https://doi.org/10.1007/s40090-019-0173-8) contains supplementary material, which is available to authorized users.

✉ Inbasekaran Muthuvel
profmuthuvelchem@yahoo.com

1 Advanced Photocatalysis Laboratory, Department of Chemistry, Annamalai University, Annamalainagar, Tamilnadu 608 002, India

2 Photocatalysis Laboratory, Department of Chemistry, M.R. Govt. Arts College, Mannargudi, Tamilnadu 614 001, India

3 Department of Chemistry, University of Coimbra, 3004-535 Coimbra, Portugal

4 Nanomaterials Laboratory, International Research Centre, Kalasalingam University, Krishnankoil, Tamilnadu 626 126, India

$Fe_2V_4O_{13}$ is also often used to degrade organic pollutants possibly because of its special two-way Fenton-like semiconductor photocatalytic mechanism of action and synergistic activation of Fe and V [12, 13]. In addition, graphene or reduced graphene oxide (RGO), reported to be a good gap linker in Z-schemes, can be coupled with various photocatalysts for increased photocatalytic efficiency [14–19]. Graphene oxide (GO) sheets contain various reactive oxygen functionalities on its surface; the oxygen functionalities have been identified as mostly hydroxyl and epoxy groups on the basal plane and smaller amounts of carboxy, carbonyl, phenol, lactone, and quinone at the sheet edges, which make GO a possible precursor for immobilization of a large number semiconductor nanoparticles [20]. Compared with graphene, GO has attracted more interest because of its easy availability in bulk quantities, readiness for functioning in chemical reactions, good dispersion in water, and high biocompatibility. Recently, we have reported $Fe_2V_4O_{13}$-assisted hetero-Fenton mineralization of methyl orange (MO) under UV light [21]. In this study, we report the synthesis of graphene oxide wrapped $Fe_2V_4O_{13}$ by the solid-state dispersion method. Further, the efficiencies of $Fe_2V_4O_{13}$ and GO/$Fe_2V_4O_{13}$ as catalysts in MO degradation under UV and solar light have been assessed.

Experimental

Synthesis of $Fe_2V_4O_{13}$

Synthesis and characterization of $Fe_2V_4O_{13}$ have been reported earlier [21]. In brief, iron nitrate aqueous solution (0.1 M) was quickly poured into an aqueous solution of NH_4VO_3 (0.2 M) and maintained at 80 °C with continuous stirring to form a yellow precipitate, and on further stirring for 3 h, the color of the precipitate changed to brown. This precipitate was then isolated by filtration, washed several times with distilled water (50 mL) and ethanol (20 mL) and dried at 100 °C for 1 h. Finally, it was calcined in a muffle furnace at 500 °C for 6 h to get $Fe_2V_4O_{13}$.

Synthesis of graphite oxide

Graphite oxide was synthesized from graphite powder by a modified Hummer's method [22]. About 4.0 g of graphite powder was first added into 92 mL of concentrated H_2SO_4 (98%) at room temperature, followed by addition of 2 g $NaNO_3$ with vigorous stirring to avoid agglomeration. The mixture was cooled to 5 °C using an ice/salt bath and the temperature of the mixture was maintained at 5 °C for 30 min. $KMnO_4$ (15.0 g) was added gradually to this mixture with stirring and cooling and, in the meanwhile, the temperature of the mixture was not allowed to reach 10 °C. At this stage, 184 mL of distilled water was added into the mixture and then stirring was continued for another 1 h. Further, 30% H_2O_2 was added to the mixture to reduce the residual $KMnO_4$. The solid obtained was filtered, washed with 5% HCl aqueous solution to remove metal ions, and washed with distilled water until the pH of the filtrate became neutral. The resulting graphite oxide was dried at 45 °C for 24 h.

Synthesis of graphene oxide (GO)

Graphite oxide (1 g) was added to 500 mL of H_2O and ultrasonically exfoliated using a bath sonicator for 1 h to achieve a light-brown precipitate. The precipitate (GO) was washed with ethanol, filtered, and dried at 80°C for 1 h.

Synthesis of GO coated with $Fe_2V_4O_{13}$

First, GO in a w/w ratio of 12, 17, 21, and 25 was sonicated in 50 mL of ethanol/water medium for 1 h to achieve uniform dispersion of GO. Next, the $Fe_2V_4O_{13}$ powder was slowly added to the GO dispersion with continuous stirring. The GO-coated $Fe_2V_4O_{13}$ mixture was further stirred for 1 h to ensure complete mixing. The precipitate was then dried at 80 °C for 2 h and used as a photocatalyst.

Photoreactor

Heber multilamp photoreactor model HML-MP 88 was used for photodegradation experiment with UV light. It consists of eight medium pressure mercury vapor lamps of 8 W, set in parallel, emitting a wavelength of 365 nm. It has a reaction chamber with specially designed reflectors made of highly polished aluminum and built-in cooling fan at the bottom. It is provided with a magnetic stirrer at the center. An open borosilicate glass tube of 40 cm height and 12.6 mm diameter was used as the reaction vessel with the total radiation exposure length of 330 mm. The irradiation was carried out using four parallel 8 W medium pressure mercury lamps in an open-air condition unit. The light intensity was measured using ferrioxalate actinometer [23] and was found to be 1.381×10^{-6} Einstein L^{-1} s^{-1}. For solar experiments, all photo-Fenton degradations have been carried out under similar conditions on sunny days of different months in 2016 between 11 a.m and 2 p.m. During the illumination period, no volatility of the solvent was observed. The intensity of solar light was measured for every 10 min and the average light intensity over the duration of each experiment was calculated. In all these experiments, the position of maximum intensity was set for the sensor. The solar light intensity was measured using LT Lutron LX-10/A digital Lux meter. The intensity of solar light $(1250\times100)\pm100$ lx was nearly constant during the experiments.

Photocatalytic degradation experiments

The dye solution (50 mL) with an appropriate quantity of the catalyst and H_2O_2 was used in all the experiments. The suspension was stirred for 30 min in dark and then it was irradiated. Continuous aeration of the dye and other solution was performed using a pump to provide oxygen and for complete mixing of the reaction medium. At regular intervals, 2–3 mL of the sample was removed from the total mixture and centrifuged to separate the catalyst. The centrifugate (1 mL) was diluted to 10 mL and its absorbance was measured at 464 nm using a UV–Vis spectrophotometer to determine the concentration of dye. From the concentration of the dye determined during the degradation process, the percentage of the dye remaining was determined. The photocatalytic degradation of MO in the presence of GO-coated $Fe_2V_4O_{13}$ catalyst obeys pseudo-first-order kinetics. At initial low dye concentration, the rate expression is given by

$$\mathrm{d}[C]/\mathrm{d}t = k'[C], \tag{5}$$

where k' is the *pseudo*-first-order rate constant. The dye is adsorbed onto the iron-immobilized catalyst surface and adsorption–desorption equilibrium is reached in 10 min. After adsorption, the equilibrium concentration of the dye solution is determined and it is taken as the initial dye concentration for kinetic analysis. Integration of Eq. 5 (with the limit of $C = C_0$ at $t = 0$ with C_0 being the equilibrium concentration of the bulk solution) gives Eq. 6

$$\ln\left(C_0/C\right) = k't, \tag{6}$$

where C_0 is the equilibrium concentration of dye and C is the concentration at time t. Pseudo-first-order rate constant k' was determined from the plot of $\ln C_0/C$ vs t.

Characterization techniques

Fourier-transform infrared spectra of the samples were recorded using Thermo Nicolet iS5 FT-IR spectrometer in KBr pellet holders. About 5 mg of sample was mixed with 50 mg of IR grade KBr, and ground and pressed using hydraulic press under a pressure of 15 tons into a wafer of 13 mm diameter. This pellet was used to record the infrared spectra in the range of 4000–400 cm^{-1}. The spectra were recorded as percentage transmittance against wavenumber. High-resolution scanning X-ray diffraction spectra were recorded on the Equinox-1000 model X-ray diffractometer from analytical instruments operated at a voltage of 30 kV and a current of 30 mA with CuKα (1.54056 Å) radiation. HR-SEM images were taken using FEI quanta FEG 250 high-resolution scanning electron microscope (Netherlands). Samples were mounted on a gold platform placed in the scanning electron microscope for taking images at various magnifications. EDX was performed at different points of the surface to minimize any possible anomalies arising from the heterogeneous nature of the analyzed surface. Most elements were detected with the concentration in the order of 0.1%. Transmission electron microscopy (TEM, JEM-2100, JEOL, Japan) was used to describe the microstructure of the sample operated at 100 keV. The samples for TEM analysis were prepared by dispersion of the catalyst in ethanol under sonication and deposition on a copper grid. Transmission electron microscopy (TEM, JEM-2100, JEOL, Japan) was used to describe the microstructure of the sample operated at 100 keV. The samples for TEM analysis were prepared by dispersion of the catalyst in ethanol under sonication and deposition on a copper grid. Ultraviolet and visible light absorbance spectra were measured over a range of 800–200 nm with a Shimadzu UV-1650PC recording spectrometer using a quartz cell with 10 mm optical path length. COD was determined using the procedure from the literature [24].

Results and discussion

FT-IR

The FT-IR spectra of $Fe_2V_4O_{13}$ and 21% GO-coated $Fe_2V_4O_{13}$ are shown in Fig. 1. The band at 1028 cm^{-1} is assigned to V–O terminal stretching vibrations and the characteristic absorption band at 711 cm^{-1} corresponds to the V–O–Fe stretching mode. The absorption band at 510 cm^{-1} is assigned to Fe–O stretching mode (Fig. 1a) [25]. In the graphene oxide/$Fe_2V_4O_{13}$ hybrid material, FT-IR spectroscopy was used to investigate the existence of oxygen-containing functionalities and their changes after impregnation. The FT-IR spectrum of GO (inset Fig. 1) exhibits the characteristic peaks for C=O (1724 cm^{-1}), aromatic C=C (1631 cm^{-1}), carboxy C–O (1417 cm^{-1}), epoxy C–O (1202 cm^{-1}), and alkoxy C–O (1096 cm^{-1}). The GO/$Fe_2V_4O_{13}$ catalyst also contains these functional groups, but the position of the bonds is slightly shifted, and the sharpness of the peaks changes indicating the change in the coordination environment of various functional groups in GO/$Fe_2V_4O_{13}$ (Fig. 1b) [26]. The peak at 1724 cm^{-1} corresponding to C=O bonding of –COOH was weaker than that of GO due to the formation of –COO– after impregnating with $Fe_2V_4O_{13}$. Moreover, the peaks at 553 cm^{-1} can be ascribed to Fe–O in $Fe_2V_4O_{13}$, suggesting that $Fe_2V_4O_{13}$ is connected with the COO^- on the edge of the GO sheets [27–29].

XRD

The XRD patterns of the prepared materials are shown in Fig. 2. The XRD pattern of the $Fe_2V_4O_{13}$ catalyst dried

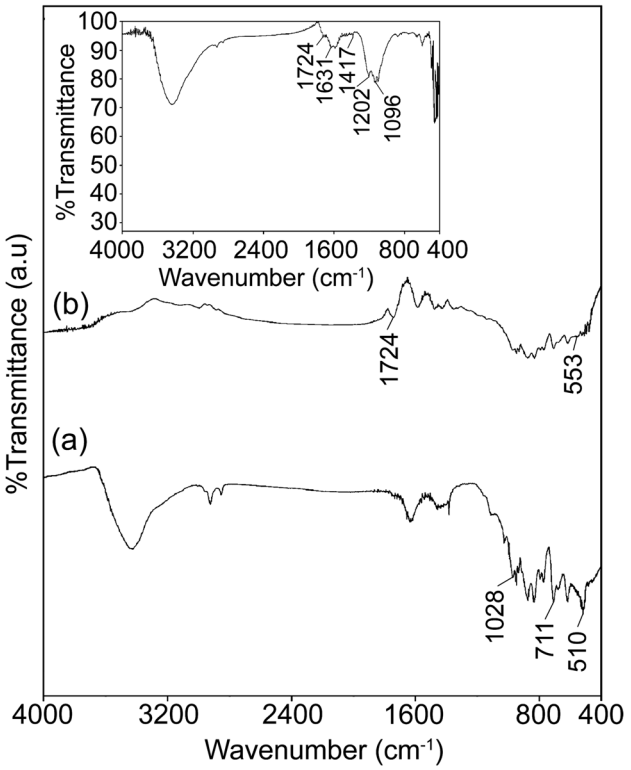

Fig. 1 FT-IR spectra of **a** $Fe_2V_4O_{13}$ and **b** 21% GO-coated $Fe_2V_4O_{13}$. Inset shows FT-IR spectrum of graphene oxide

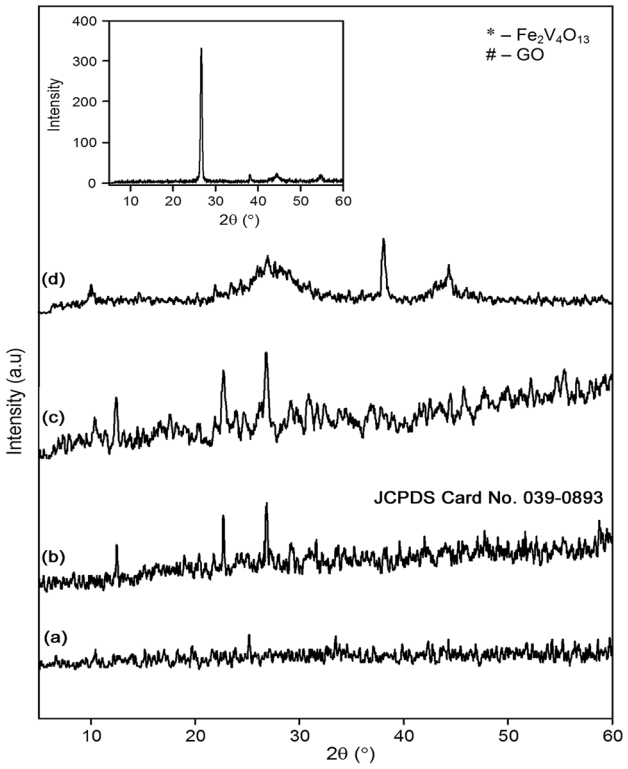

Fig. 2 XRD patterns of **a** $Fe_2V_4O_{13}$ (100 °C), **b** $Fe_2V_4O_{13}$ (500 °C), **c** 21% GO-coated $Fe_2V_4O_{13}$ and **d** GO. Inset shows XRD pattern of graphite powder

at 100 °C presented a weak peak at the 2θ angle of about 25° (Fig. 2a), suggesting that the solid catalyst is a kind of amorphous compound [30]. At 500 °C, the catalyst has three intense peaks (Fig. 2b). The diffraction peaks are well matched with the diffraction peaks distinctly observed at the 2θ angle of 12.5°, 22.7°, and 26.7° monoclinic phase of $Fe_2V_4O_{13}$ (JCPDS no. 00-039-0893). The strong and narrow diffraction peaks demonstrated good crystallinity. Figure 2c shows the XRD pattern for 21% GO coated on $Fe_2V_4O_{13}$, which has the same diffraction peaks at 12.5°, 22.7°, and 26.7° as that of the $Fe_2V_4O_{13}$ catalyst and a slightly weak diffraction peak observed at 10.8° indicating a very small amount of GO coated on the $Fe_2V_4O_{13}$. The graphite displays a characteristic peak at $2\theta = 26.5°$ with a corresponding *d*-spacing of 3.35 Å indicating the index of (002) (inset Fig. 2). After oxidation, the characteristic graphite peaks disappeared and were replaced by a well-defined peak at $2\theta = 10.8°$ (Fig. 2d) with the *d*-spacing of 8.16 Å, and this is due to the presence of copious oxygen-containing functional groups. This value indicates that the distance between the graphene sheets has increased due to the insertion of interplanar groups. The broad peak observed in the exfoliated GO sample (Fig. 2d) suggests very poor ordering along the stacking direction and implies that these samples are composed mostly of free graphene sheets [31].

HR-SEM with EDX

HR-SEM images of $Fe_2V_4O_{13}$ and 21% GO-coated $Fe_2V_4O_{13}$ are shown in Fig. 3. These images show a flaky structure in both cases; however, aggregation (or) interconnection appeared when $Fe_2V_4O_{13}$ (Fig. 3) was thermally heated at 500 °C for 6 h. The corresponding energy dispersive X-ray (EDX) spectra demonstrate the presence of the Fe, V, and O in the $Fe_2V_4O_{13}$ and 21% GO/$Fe_2V_4O_{13}$ catalysts (Figs. S1a and S1b, see supplementary material). Moreover, the increase of at % and wt % of C in the case of 21% GO/$Fe_2V_4O_{13}$ (inset Fig. S1b) reveals the presence of GO in GO/$Fe_2V_4O_{13}$.

TEM

TEM images of 21% GO-coated $Fe_2V_4O_{13}$ at different magnifications (Fig. 4a–c) are shown in Fig. 4. It is found that the GO-coated $Fe_2V_4O_{13}$ particle sizes range from 8 to 15 nm. It has been reported that the structure of $Fe_2V_4O_{13}$ aggregated when it was annealed at 400 °C [32]. The obtained composite retained the two-dimensional sheet structure. It can be seen from Fig. 4 that there is a nice dispersion of nanosized $Fe_2V_4O_{13}$ particles on the surface of the graphene sheet support. The TEM characterization

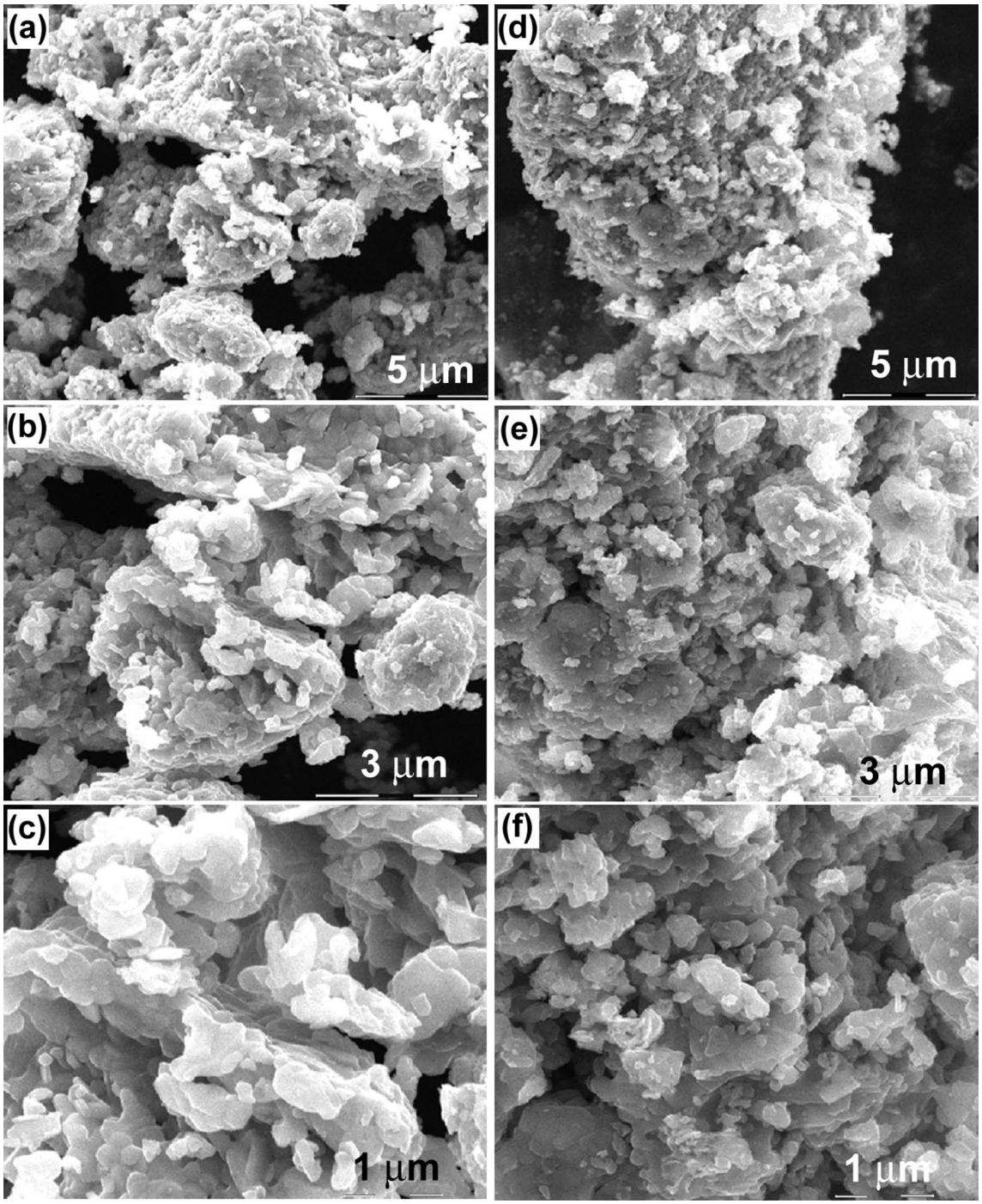

Fig. 3 HR-SEM images of $Fe_2V_4O_{13}$: **a** 5 μm, **b** 3 μm, **c** 1 μm and 21% GO coated $Fe_2V_4O_{13}$: **d** 5 μm, **e** 3 μm, **f** 1 μm

suggests the formation of a good interfacial contact between the $Fe_2V_4O_{13}$ nanoparticles and the 2D graphene sheet. The transfer process of charge carriers in graphene semiconductor nanocomposites is intimately related with the interfacial interaction between graphene and the semiconductor [33–37].

UV-DRS

The absorbance spectrum illustrates that the absorption edge of the $Fe_2V_4O_{13}$ catalyst extends to the visible region (around 580 nm), which suggests the possibility of photoactivity of this material under visible light (Fig. 5a). The 21% GO/$Fe_2V_4O_{13}$

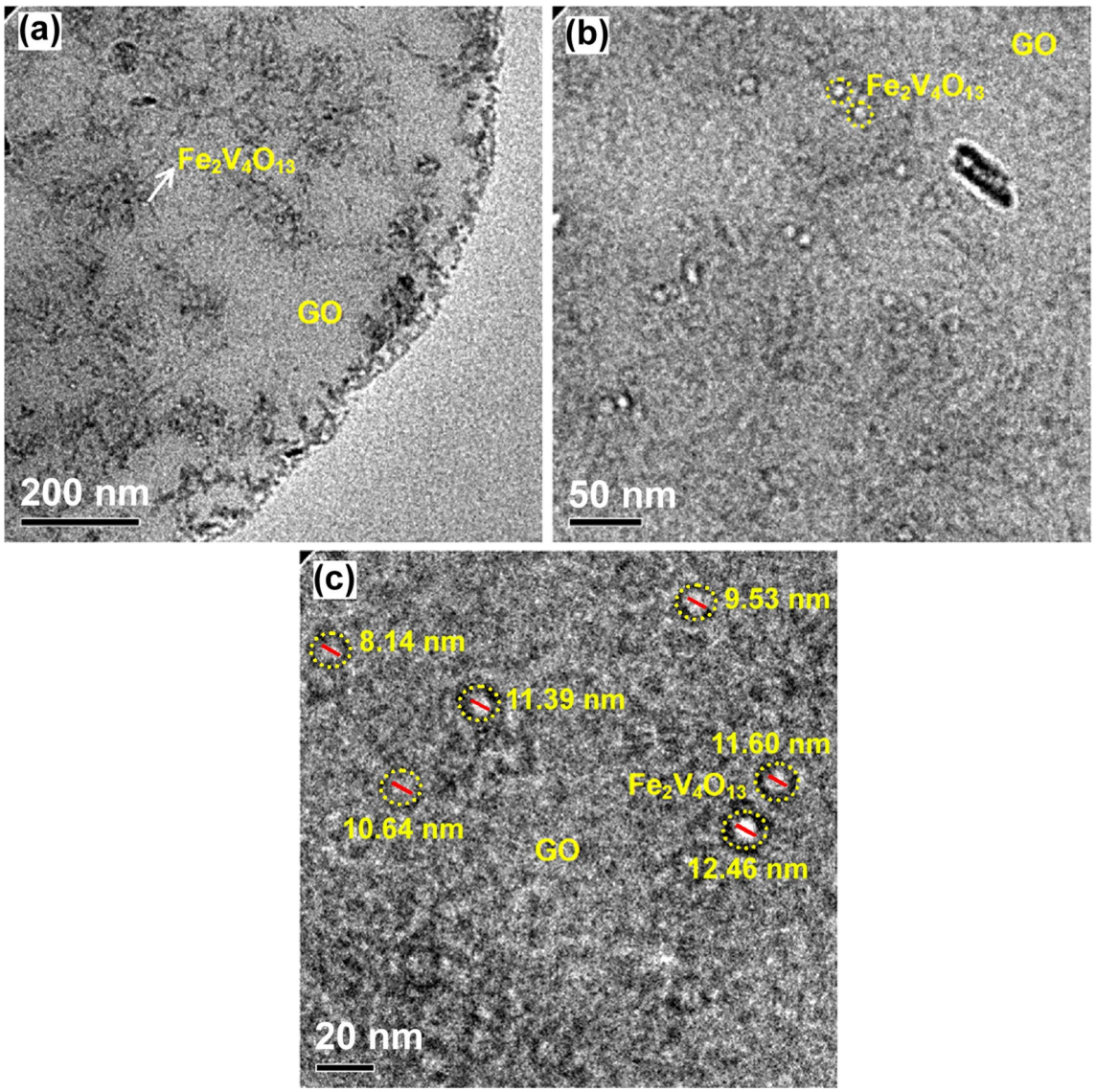

Fig. 4 TEM images of 21% GO-coated $Fe_2V_4O_{13}$: **a** 200 nm, **b** 50 nm and **c** 20 nm

sample also has increased absorption in the UV–visible region (200–500 nm) and its absorption edge is extended up to 650 nm (Fig. 5b). This may be due to the presence of GO in the catalyst. Kubelka–Munk analyses for allowed direct band gaps for $Fe_2V_4O_{13}$ and 21% GO-coated $Fe_2V_4O_{13}$ are shown in insets of Fig. 5a and b, respectively. The estimated optical band gaps of $Fe_2V_4O_{13}$ and GO/$Fe_2V_4O_{13}$ are ~ 2.21 and 2.19 eV, respectively.

Influence of process parameters on photodegradation of MO with GO/$Fe_2V_4O_{13}$ catalyst by UV light

Effect of graphene oxide amount on $Fe_2V_4O_{13}$

The optimum GO loading on $Fe_2V_4O_{13}$ was investigated by varying the amount of GO from 12 to 25 by wt % in

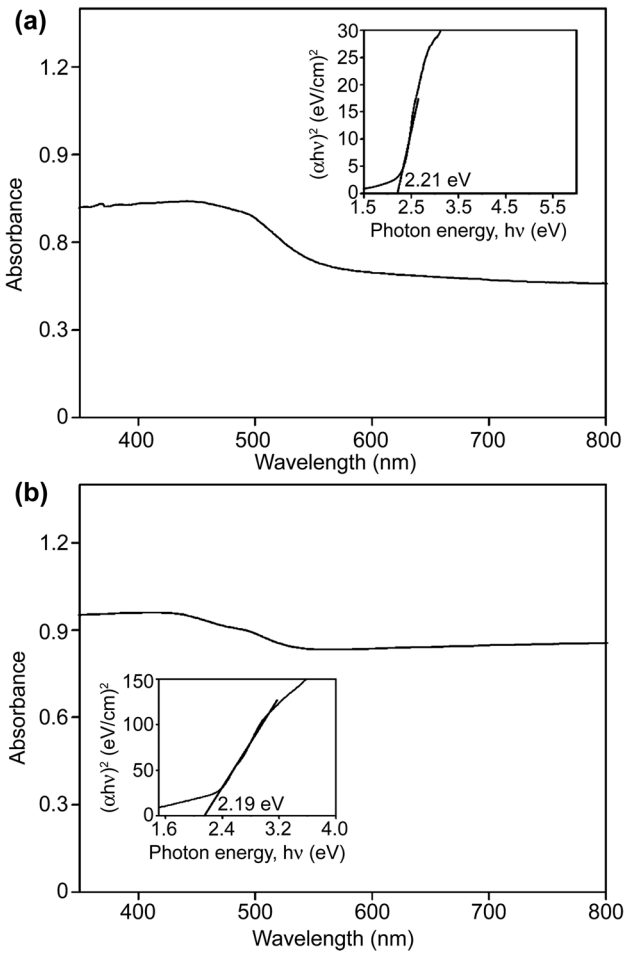

Fig. 5 DRS of **a** $Fe_2V_4O_{13}$ and **b** 21% GO coated $Fe_2V_4O_{13}$. Inset shows the plot of $(\alpha h\nu)^2$ (eV/cm)^2 Vs $h\nu$ (eV) for determining band gap energy of $Fe_2V_4O_{13}$ and 21% GO-coated $Fe_2V_4O_{13}$

the preparation of the GO/$Fe_2V_4O_{13}$ composite catalysts. These composite catalysts were used for photodegradation of MO. As the amount of GO increased from 12 to 21 wt %, the rate of degradation increased from 0.023 to 0.052 min^{-1} (Fig. 6); this is mainly because of the increase in the amount of the GO on the $Fe_2V_4O_{13}$ catalyst, which in turn increases the presence of active sites on the catalyst surface. Moreover, more GO on $Fe_2V_4O_{13}$ catalyst could increase the adsorption of MO, which would be due to the oxygen-containing functionalities on the surface of the catalyst. Further increases of GO content decrease the rate of degradation (25%, 0.038 min^{-1}) and this may be due to the blockage of active sites by an excess amount of GO. Under this same condition, the rate of MO degradation under UV light with pristine $Fe_2V_4O_{13}$ is 0.0287 min^{-1} [21]. Hence, 21% GO on $Fe_2V_4O_{13}$ is the optimum amount of GO on $Fe_2V_4O_{13}$ for the mineralization of MO.

Effect of H_2O_2 concentration

The results of H_2O_2 addition at concentrations ranging from 5 to 20 mmol on the heterophoto-Fenton mineralization are shown in Fig. 7. The addition of H_2O_2 from 5 to 15 mmol increases the degradation rate constant from 0.009 to 0.071 min^{-1}. Above 15 mmol, the degradation rate constant decreases. Hence, H_2O_2 concentration of 15 mmol appears to be optimal for the degradation process. The enhancement of mineralization by the addition of H_2O_2 is due to the increased production of hydroxyl radicals (Eqs. 7 and 8).

$$H_2O_2 + e^-_{CB} \rightarrow {}^{\cdot}OH + OH^- \quad (7)$$

$$H_2O_2 + {}^{\cdot}O_2^- \rightarrow {}^{\cdot}OH + H^+ + O_2 \quad (8)$$

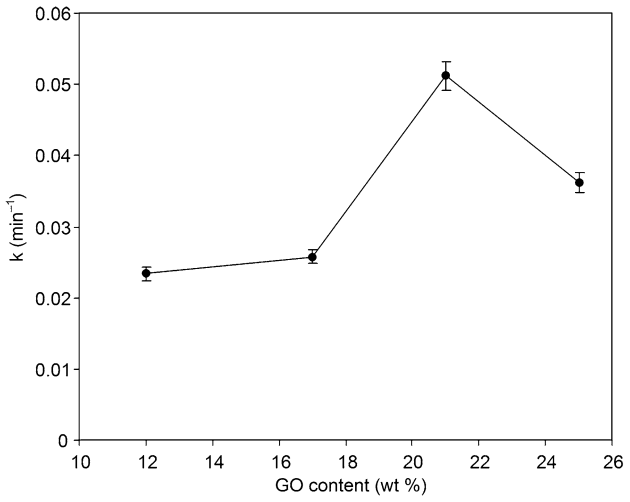

Fig. 6 Effect of GO coated on $Fe_2V_4O_{13}$. [MO] = 4×10^{-4} M, catalyst suspended = 0.600 g L^{-1}, H_2O_2 = 10 mmol, airflow rate = 8.1 mL s^{-1}, pH = 6.0, $I_0 = 1.381\times10^{-6}$ einstein L^{-1} s^{-1}

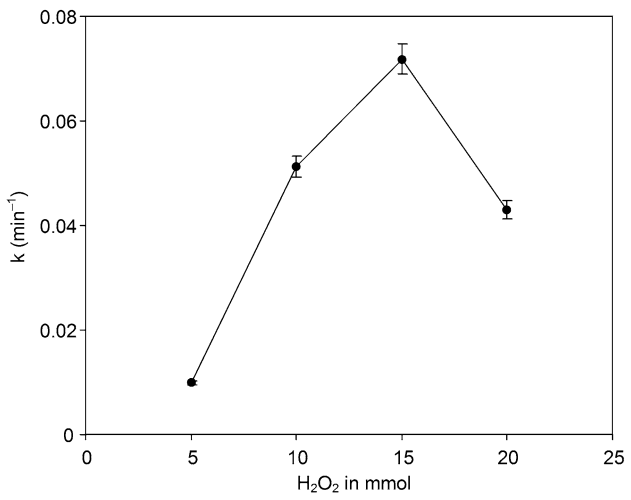

Fig. 7 Effect of H_2O_2 dosage. [MO] = 4×10^{-4} M, 21% GO/$Fe_2V_4O_{13}$ = 0.600 g L^{-1}, airflow rate = 8.1 mL s^{-1}, pH = 6.0, $I_0 = 1.381\times10^{-6}$ einstein L^{-1} s^{-1}

At H_2O_2 concentration above 15 mmol, the decrease in the removal rate of the dye is due to decrease in hydroxyl radicals and hole-scavenging effect of H_2O_2 (Eqs. 9 to 11).

$$H_2O_2 + {}^{\cdot}OH \rightarrow HO_2^{\cdot} + H_2O \quad (9)$$

$$HO_2^{\cdot} + {}^{\cdot}OH \rightarrow H_2O + O_2 \quad (10)$$

$$H_2O_2 + h_{nB} \rightarrow HO_2^{\cdot} + H^+ \quad (11)$$

Effect of initial solution pH

The effect of initial solution pH on the degradation of MO is shown in Fig. S2. At pH 6, 95% degradation was obtained (40 min) in the heterophoto-Fenton process with 15 mmol of H_2O_2, and its efficiency decreased when the initial pH of the solution changed from pH 6. Hence, the highest activity was observed at pH 6. Since the photocatalytic efficiency depends on the adsorption of the dye onto the surface of the catalyst, the adsorption of the dye under different pH values was investigated. After the adsorption–desorption equilibrium of MO with GO/$Fe_2V_4O_{13}$ in the dark, the adsorption capacities are 15, 18, 28, 5, 4, and 10% for pH 4, 5, 6, 7, 8, and 9, respectively. As the adsorption is high at pH 6, the degradation is also efficient at this pH. The results show that the GO/$Fe_2V_4O_{13}$ catalyst has a high adsorption capacity for MO, which is in favor of the increased photocatalytic activity compared to $Fe_2V_4O_{13}$.

Effect of initial dye concentration

The effect of the initial concentration of MO on the photo-Fenton degradation rate was investigated over a concentration range from 1 to 5×10^{-4} M. Increase in the initial dye concentration from 1 to 5×10^{-4} M decreases the degradation rate constant from 0.105 to 0.011 min^{-1} (20 min) (Fig. S3). The rate of degradation relates to the ${}^{\cdot}OH$ (hydroxyl radical) formation on the catalyst surface and the probability of ${}^{\cdot}OH$ reacting with the dye molecule. For all initial dye concentrations, the catalyst amount and light intensity are same. Since the generation of hydroxyl radical remains constant, the probability of dye molecule reacting with hydroxyl radicals decreases. In the photo-Fenton process, at higher dye concentrations, the penetration of photons into the solution also decreases, thereby lowering the hydroxyl radical productionand, hence, the decrease in percentages of degradation with an increase in dye concentration [38, 39].

Long-term stability

Stability of the catalysts was tested in the degradation of MO. Fig. S4 shows the degradation of MO using the GO/$Fe_2V_4O_{13}$ catalyst in five consecutive photo-Fenton experiments. The percentages of degradation for 50 min in the first, second, third, fourth, and fifth runs are 98, 96, 96, 96, and 96, respectively. There was no significant decrease in degradation efficiency observed for all runs. Hence, the catalyst is highly stable and reusable.

COD measurements

As the reduction of chemical oxygen demand (COD) reflects the extent of degradation or mineralization of an organic species, the percentage change in COD was determined for the dye sample (initial concentration 4×10^{-4} M) under optimum conditions. The percentages of COD reduction were 70 and 82 with $Fe_2V_4O_{13}$ and GO/$Fe_2V_4O_{13}$, respectively, after 60 min irradiation (Table 1). Degradations of MO of about 80% with $Fe_2V_4O_{13}$ and 88% with GO/$Fe_2V_4O_{13}$ were observed at 40 min irradiation by absorbance measurements, whereas only 70% and 82% mineralizations were observed at 60 min irradiation by COD measurements under the same conditions. This reveals the presence of nonabsorbing organic intermediates at 40 min. Hence, complete mineralization may be achieved at 90 min of irradiation.

Comparison of photodegradation of MO using $Fe_2V_4O_{13}$ and 21% GO/$Fe_2V_4O_{13}$ under UV and solar light

Solar experiments were carried out at various pH, ranging from 4 to 9 with a constant concentration of the dye (4×10^{-4} M) and the catalysts $Fe_2V_4O_{13}$ and 21% GO/$Fe_2V_4O_{13}$ (0.600 g L^{-1}). $Fe_2V_4O_{13}$ shows an increase in the degradation from 75 to 98% for the increase of pH from 4 to 6 (Fig. 8a). Similarly, 21% GO/$Fe_2V_4O_{13}$ catalyst shows a maximum degradation efficiency of 99% at pH 6 (Fig. 8b). Further increase of pH above 6 for both catalysts decreases the degradation efficiency.

The percentage of photodegradation of 4×10^{-4} M of MO using $Fe_2V_4O_{13}$ and GO/$Fe_2V_4O_{13}$ catalyst by UV and solar light under optimum conditions at 40 min irradiation is given in Table 2. The degradation efficiencies of the above two processes are in the following order: The solar process has higher efficiency compared to the UV process with both catalysts.

Table 1 COD measurements under optimum conditions

Catalyst	COD reduction (%)
$Fe_2V_4O_{13}$	70
21% GO/$Fe_2V_4O_{13}$	82

[MO] = 4×10^{-4} M, H_2O_2 = $Fe_2V_4O_{13}$ (10 mmol), 21% GO/$Fe_2V_4O_{13}$ (15 mmol), catalyst suspended = 0.600 g L^{-1}, pH = 6.0, airflow rate = 8.1 mL s^{-1}

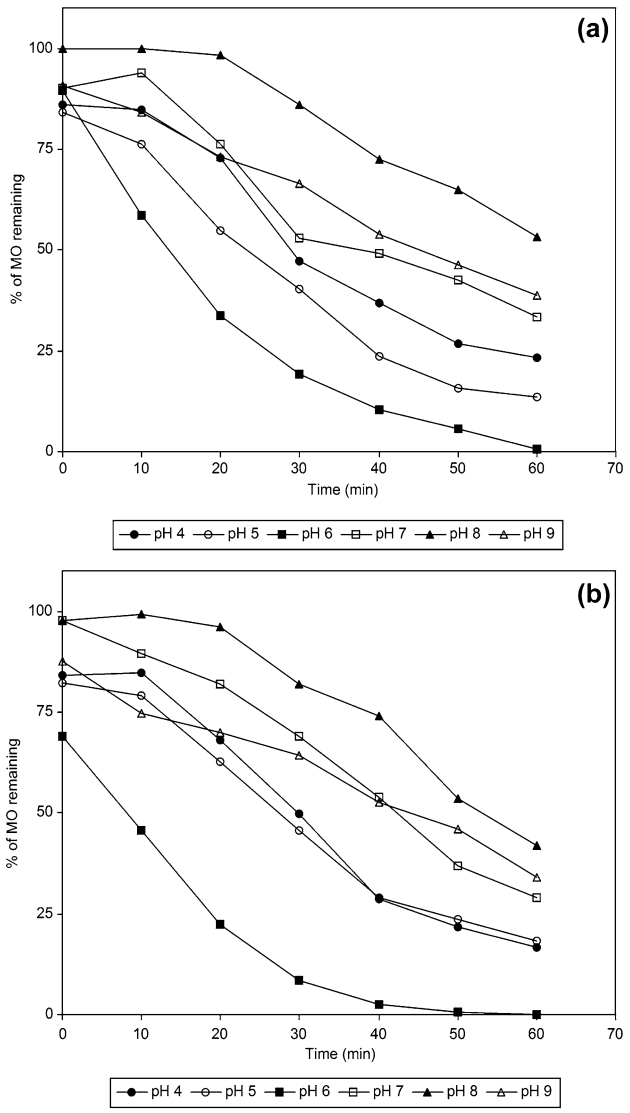

Fig. 8 Effect of initial solution pH (solar). **a** [MO] = 4×10^{-4} M, $Fe_2V_4O_{13}$ = 0.600 g L^{-1}, H_2O_2 = 10 mmol, airflow rate = 8.1 mL s^{-1} and **b** [MO] = 4×10^{-4} M, 21% GO/$Fe_2V_4O_{13}$ = 0.600 g L^{-1}, H_2O_2 = 15 mmol, airflow rate = 8.1 mL s^{-1}

Solar	>	UV	>	Solar	>	UV
21% GO/ $Fe_2V_4O_{13}$		21% GO/ $Fe_2V_4O_{13}$		$Fe_2V_4O_{13}$		$Fe_2V_4O_{13}$

Proposed mechanism

The enhancement of the efficiency of the 21% GO/$Fe_2V_4O_{13}$ composite in the degradation of methyl orange (MO) presumably results from the following reasons. Firstly, graphene oxide (GO) improves the adsorption of dye and H_2O_2 due to its large surface area and the presence of oxygen-containing functionalities on the surface of the catalyst. Secondly, H_2O_2 can act as an efficient electron scavenger to form $^{\cdot}OH$ on the surface of the graphene oxides, which not only enhances oxidation ability but also fleetingly reduces electronic accumulation on the surface of graphene oxides. Furthermore, the high catalytic activity brought about by $Fe_2V_4O_{13}$ in 21% GO/$Fe_2V_4O_{13}$ partly contributes to the two-way catalytic mechanism involved in the Fe(III)/Fe(II) and V(V)/V(IV) redox couples [21]. Generally, in heterogeneous Fenton-like catalysts, a Lewis acid, which is associated with iron, could facilitate the reduction of the ferric ion by H_2O_2 attracting the electron density from the iron center. This facilitation will accelerate the whole Fenton-like reaction as the reduction of ferric ion is the dominant rate-determining step of the Fenton-like reaction. In $Fe_2V_4O_{13}$, V(V) has many positive charges and is a strong Lewis acid. Hence, V(V) can facilitate the reduction of Fe(III), sequentially leading to the enhancement of the overall MO degradation rate [21]. Therefore, the GO/$Fe_2V_4O_{13}$ hybrid composite exhibits enhanced photocatalytic activity under UV and solar irradiation in the presence of H_2O_2 (Fig. 9).

Table 2 Comparison of photodegradation of MO using $Fe_2V_4O_{13}$ and 21% GO/$Fe_2V_4O_{13}$ under UV and solar light

Catalyst	Degradation (%)	
	UV	Solar
$Fe_2V_4O_{13}$	80.9	88.6
21% GO/$Fe_2V_4O_{13}$	90.1	91.2

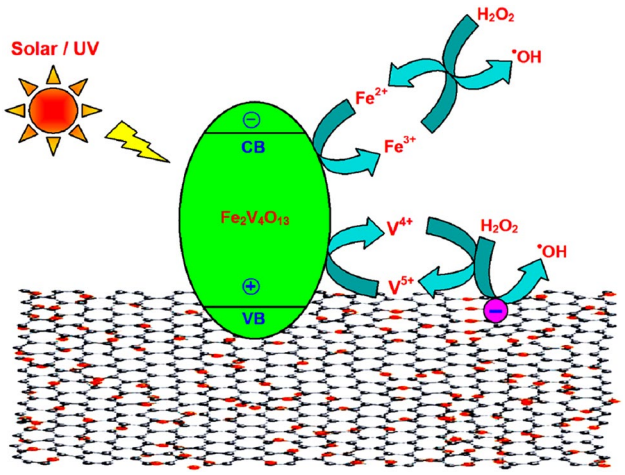

Fig. 9 Mechanism for 21% GO coated $Fe_2V_4O_{13}$ in the presence of MO under UV and solar light

Conclusion

Heterogeneous Fenton-like catalysts $Fe_2V_4O_{13}$ and 21% GO/$Fe_2V_4O_{13}$, prepared by the solid-state dispersion method, were used for the degradation of methyl orange (MO) under UV light. The characterization study revealed the presence of monoclinic phase of $Fe_2V_4O_{13}$ in the catalyst and the homogeneous dispersion of nanosized $Fe_2V_4O_{13}$ particles on the surface of the graphene oxide. The particle sizes range from 20 to 100 nm. A mechanism for the heterophoto-Fenton process is also proposed. Both catalysts show maximum degradation efficiency at pH 6 and the solar process is more efficient than the UV process in both catalysts. From this study, it is found that $Fe_2V_4O_{13}$ and 21% GO/$Fe_2V_4O_{13}$ catalysts are efficient under both UV and solar light for the degradation MO and they can be used for the treatment of wastewater contaminated with dye.

Acknowledgements One of the authors (I. Muthuvel) thank financial support from the University Grants Commission (UGC), New Delhi, for through research grant No. UGC sanctioned letter F.No-43-222/2014(SR). This work was supported by FCT post doc Grant SFRH/BPD/86971/2012 (B. Krishnakumar).

References

1. Yu J, Yu JC, Leung MKP, Ho W (2003) Effects of acidic and basic hydrolysis catalysts on the photocatalytic activity and microstructures of bimodal mesoporous titania. J Catal 217:69–78
2. Hoffmann MR, Martin ST, Choi WY, Bahnemann DW (1995) Environmental applications of semiconductor photocatalysis. Chem Rev 95:69–96
3. Zhang C, Zhu YF (2005) Synthesis of square Bi_2WO_6 nanoplates as high-activity visible-light-driven photocatalysts. Chem Mater 17:3537–3545
4. Wang X, Lian W, Fu X, Basset JM, Lefebvre F (2006) Structure, preparation and photocatalytic activity of titanium oxides on MCM-41 surface. J Catal 238:13–20
5. Cesar L, Kay A, Martinez JAG, Gratzel M (2006) Translucent thin film Fe_2O_3 photoanodes for efficient water splitting by sunlight: nanostructure-directing effect of Si-doping. J Am Chem Soc 128:4582–4583
6. Chen SF, Chen L, Gao S, Cao GY (2005) The preparation of nitrogen-doped photocatalyst $TiO_{2-X}N_X$ by ball milling. Chem Phys Lett 413:404–409
7. Gomathi Devi L, Girish Kumar S (2011) Strategies developed on the modification of titania for visible light response with enhanced interfacial charge transfer process: an overview. Cent Eur J Chem 9:959–961
8. Muruganandham M, Selvam K, Swaminathan M (2007) A comparative study of quantum yield and electrical energy per order (E_{Eo}) for advanced oxidative decolourisation of reactive azo dyes by UV light. J Hazard Mater 144:316–322
9. Neyens E, Baeyens J (2003) A review of classic Fenton's peroxidation as an advanced oxidation technique. J Hazard Mater 98:33–50
10. Muthuvel I, Swaminathan M (2007) Photoassisted Fenton mineralization of Acid Violet 7 by heterogeneous Fe(III)-Al_2O_3 catalyst. Catal Commun 8:981–986
11. Herney-Ramirez J, Lampinen M, Vicente MA, Costa CA, Madeira LM (2008) Experimental design to optimize the oxidation of Orange II dye solution using a clay-based Fenton-like catalyst. Ind Eng Chem Res 47:284–294
12. Zhang YY, He C, Deng JH, Tu YT, Liu JK, Xiong Y (2009) Photo-Fenton-like catalytic activity of nano-lamellar $Fe_2V_4O_{13}$ in the degradation of organic pollutants. Res Chem Intermed 35:727–737
13. Zhang YY, Deng JH, He C, Huang SS, Tian SH, Xiong Y (2010) Application of $Fe_2V_4O_{13}$ as a new multi-metal heterogeneous Fenton-like catalyst for the degradation of organic pollutants. Environ Technol 31:145–154
14. Iwase A, Ng YH, Ishiguro Y, Kudo A, Amal R (2011) Reduced graphene oxide as a solid-state electron mediator in Z-scheme photocatalytic water splitting under visible light. J Am Chem Soc 133:11054–11057
15. Wang X, Yin L, Liu G (2014) Light irradiation-assisted synthesis of ZnO–CdS/reduced graphene oxide heterostructured sheets for efficient photocatalytic H_2 evolution. Chem Commun 50:3460–3463
16. Wang Y, Wang F, He J (2013) Controlled fabrication and photocatalytic properties of a three-dimensional ZnO nanowire/reduced graphene oxide/CdS heterostructure on carbon cloth. Nanoscale 5:11291–11297
17. Tu W, Zhou Y, Zou Z (2013) Versatile graphene-promoting photocatalytic performance of semiconductors: basic principles, synthesis, solar energy conversion, and environmental applications. Adv Funct Mater 23:4996–5008
18. Li P, Zhou Y, Li H, Xu Q, Meng X, Wang X, Xiao M, Zou Z (2015) All-solid-state Z-scheme system arrays of $Fe_2V_4O_{13}$/RGO/CdS for visible light-driving photocatalytic CO_2 reduction into renewable hydrocarbon fuel. Chem Commun 51:800–803
19. Tatykayev B, Donat F, Alem H, Balan L, Medjahdi G, Uralbekov B, Schneider R (2017) Synthesis of core/shell ZnO/rGO nanoparticles by calcination of ZIF-8/rGO composites and their photocatalytic activity. ACS Omega 2:4946–4954
20. Kassaee MZ, Motamedi E, Majdi M (2011) Magnetic Fe_3O_4-graphene oxide/polystyrene: fabrication and characterization of a promising nanocomposite. Chem Eng J 172:540–549
21. Gowthami K, Suppuraj P, Thirunarayanan G, Krishnakumar B, Sobral AJFN, Swaminathan M, Muthuvel I (2018) $Fe_2V_4O_{13}$ assisted hetero-Fenton mineralization of methyl orange under UV-A light irradiation. Iranian Chem Commun 6:97–108
22. Hummers WS, Offeman RE (1958) Preparation of graphitic oxide. J Am Chem Soc 80:1339
23. Kuhn HJ, Braslavsky SE, Schmidt R (2004) Organic and biomolecular chemistry division subcommittee on photochemistry, Chemical actinometry (IUPAC Technical Report). Pure Appl Chem 76:2105–2146
24. Muthuvel I, Krishnakumar B, Swaminathan M (2014) UV-A/solar light induced Fenton mineralization of Acid Red 1 using Fe modified bentonite composite. Indian J Chem 53A:672–678
25. Li P, Zhou Y, Tu W, Liu Q, Yan S, Zou Z (2013) Direct growth of $Fe_2V_4O_{13}$ nanoribbons on a stainless-steel mesh for visible-light

photoreduction of CO_2 into renewable hydrocarbon fuel and degradation of gaseous isopropyl alcohol. ChemPlusChem 78:274–278
26. Guo S, Zhang G, Guo Y, Yu JC (2013) Graphene oxide-Fe_2O_3 hybrid material as highly efficient heterogeneous catalyst for degradation of organic contaminants. Carbon 60:437–444
27. Deltche CR, Franck R, Cabuil V, Massart R (1987) Surfacted ferrofluids: interactions at the surfactant-magnetic iron oxide interface. J Chem Res 5:126–127
28. Chin SF, Iyer KS, Raston CL (2008) Fabrication of carbon nanotubes decorated with ultra fine superparamagnetic nano-particles under continuous flow conditions. Lab Chip 8:439–442
29. Yang XY, Zhang XY, Ma YF, Huang Y, Wang YS, Chen YS (2009) Superparamagnetic graphene oxide-Fe_3O_4 nanoparticles hybrid for controlled targeted drug carriers. J Mater Chem 19:2710–2714
30. Baudrin E, Denis S, Orsini F, Seguin L, Touboul M, Tarascon JM (1999) On the synthesis of monovalent, divalent and trivalent element vanadates. J Mater Chem 9:101–105
31. Karthika P, Rajalakshmi N, Dhathathreyan KS (2012) Functionalized exfoliated graphene oxide as supercapacitor electrodes. Soft Nanosci Lett 2:59–66
32. Si Y, Zhao L, Yu Z, Wang W, Qiu J, Yang Y (2012) A novel amorphous $Fe_2V_4O_{13}$ as cathode material for lithium secondary batteries. Mater Lett 72:145–147
33. Zhang Y, Tang ZR, Fu X, Xu YJ (2011) Engineering the unique 2D mat of graphene to achieve graphene-TiO_2 nanocomposite for photocatalytic selective transformation: what advantage does graphene have over its forebear carbon nanotube? ACS Nano 5:7426–7435
34. Zhang Y, Zhang N, Tang ZR, Xu YJ (2012) Graphene transforms wide band gap ZnS to a visible light photocatalyst. The new role of graphene as a macromolecular photosensitizer. ACS Nano 6:9777–9789
35. Zhang Y, Zhang N, Tang ZR, Xu YJ (2012) Improving the photocatalytic performance of graphene-TiO_2 nanocomposites via a combined strategy of decreasing defects of graphene and increasing interfacial contact. Phys Chem Chem Phys 14:9167–9175
36. Liang YT, Vijayan BK, Gray KA, Hersam MC (2011) Minimizing graphene defects enhances titania nanocomposite-based photocatalytic reduction of CO_2 for improved solar fuel production. Nano Lett 11:2865–2870
37. Liang YT, Vijayan BK, Lyandres O, Gray KA, Hersam MC (2012) Effect of dimensionality on the photocatalytic behavior of carbon-titania nanosheet composites: charge transfer at nanomaterial interfaces. J Phys Chem Lett 3:1760–1765
38. Muthuvel I, Krishnakumar B, Swaminathan M (2012) Novel Fe encapsulated montmorillonite K10 clay for photo-Fenton mineralization of Acid Yellow 17. Indian J Chem 51A:800–806
39. Krishnakumar B, Swaminathan M (2011) Influence of operational parameters on photocatalytic degradation of a genotoxic azo dye Acid Violet 7 in aqueous ZnO suspensions. Spectrochim Acta A 81:739–744